J Nanostruct 16(3): 3136-3152, Summer 2026

RESEARCH PAPER

Taguchi-optimized synthesis of a SiO_2-reinforced Sa-g-poly(AAM-co-CA) nanocomposite hydrogel for enhanced adsorption of Pb^{2+} ions: kinetic, isotherm, and thermodynamic studies

Ali H. Jafat [1]*, *Nadher D. Radia* [2]

[1] *Ministry of Education, General Directorate of Education of Karbala, Karbala, Iraq*

[2] *Department of Chemistry, College of Education, University of Al-Qadisiyah, Al-Qadisiyah, Iraq*

ARTICLE INFO

Article History:
Received 14 March 2026
Accepted 12 May 2026
Published 01 July 2026

Keywords:
Adsorption
Hydrogel
Lead removal
SiO_2 Nano
Taguchi

ABSTRACT

Hydrogels were synthesized via free-radical polymerization using sodium-g-poly(acrylamide-crotonic acid) alginate, with reactant concentrations optimized using the Taguchi method. Furthermore, a nano-hydrogel was prepared by adding silica nanoparticles. The hydrogel and nanocomposite were characterized using FTIR, FESEM-EDX, TEM, XRD, TGA, and BET-BJH spectroscopy. The study focused on the removal of lead (Pb^{2+}) ions from aqueous solutions. The maximum adsorption capacity was 243.667 mg/g at 35 °C, and the adsorption kinetics were found to be consistent with a pseudo-second-order reaction model. Moreover, the adsorption of lead (Pb^{2+}) ions followed Freundlich and Temkin isothermic patterns. The Pb^{2+} removal study at different temperatures (5, 15, 25, and 35 °C) demonstrated that the adsorption process is primarily a physical one. Gibbs free energy, enthalpy, entropy, and equilibrium constant were calculated. In this study, we investigated the effects of both temperature and pH. The results showed that with increasing pH and temperature, adsorption efficiency increased, consistent with the endothermic nature of the process, which was spontaneous. The Pb^{2+} removal efficiency was verified after washing the adsorbent with sodium hydroxide, and the results were very encouraging, even after five washes.

How to cite this article
H. Jafat A., D. Radia N. Taguchi-optimized synthesis of a SiO_2-reinforced Sa-g-poly(AAM-co-CA) nanocomposite hydrogel for enhanced adsorption of Pb^2+ ions: kinetic, isotherm, and thermodynamic studies. J Nanostruct, 2026; 16(3):3136-3152. DOI: 10.22052/JNS.2026.03.010

INTRODUCTION

Water is essential for life; no living organism can survive without it. However, with rapid industrial development, rivers and other freshwater sources have become increasingly vulnerable to pollution from heavy metals such as cadmium, lead, copper, and others. This pollution disrupts the ecological balance and poses a threat to all living organisms, including humans. This pollution is attributed to various industrial activities, most notably mining, oil production, and glass manufacturing [1,2]. Because it is not biodegradable and is prone to bioaccumulation, researchers have turned to developing and applying several methods to reduce and treat this type of pollution [3]. Lead is found in wastewater generated from a wide range

* *Corresponding Author Email: ali.chem.post2@qu.edu.iq*

of industries, such as electroplating processes, nickel-cadmium battery manufacturing, fertilizer and pesticide production, dye manufacturing, and textile industries [4]. Lead ions (Pb^{2+}) are a serious health and environmental pollutant, primarily affecting the liver and nervous system. Their toxicity stems in part from their mimicry of divalent metal ions such as calcium, disrupting cellular functions and vital signaling pathways [5]. Lead ions (Pb^{2+}) lead to cellular dysfunction by inducing oxidative stress and mitochondrial disruption, including inhibition of respiratory complexes, increased reactive oxygen species, and stimulation of mitochondrial permeability, which may lead to cell death [6]. In addition, the toxic effects of lead ions (Pb^{2+}) increase when present with other agents that affect mitochondria, such as FCCP and RuRed, impairing cell viability through mechanisms that go beyond ion absorption alone [7]. Research focuses on removing lead from contaminated water. Traditional methods include reduction, precipitation, ion exchange, filtration, electrochemical treatment, and membrane technology; however, their effectiveness may decrease or their cost increase at low concentrations of metals. Adsorption is a promising method because it is low-cost, easy to prepare, low-toxicity, and biodegradable. Its efficiency can be improved by selecting the type of adsorbent, the nature of the active groups, and the surrounding environmental conditions, enabling effective adsorption of pollutants under varying conditions [8]. Methods for preparing absorbent materials vary depending on their type, including some unprocessed natural materials such as chitosan, cellulose, and polysaccharides, which are used as effective media for the adsorption of heavy metals from water, thus enabling sustainable and economical treatment of mineral pollution [9,10]. Alternatively, the absorbent materials can be entirely synthetic, prepared from synthetic monomers such as poly acrylic acid, allowing control over their chemical and physical properties to enhance adsorption efficiency [11]. Using modeling in the preparation of composite materials, through software that provides comprehensive statistical analysis of the effect of changing component concentrations on the composition of the composite and its adsorption or swelling efficiency, contributes to achieving higher accuracy compared to traditional methods. One of the most prominent of these methods is the Taguchi method, which reduces the number of experiments while maintaining accurate and reliable results [12,13]. In addition, a number of statistical methods and models were employed to simulate the adsorption process and to study the effect of the various variables controlling it [14]. Hydrogels are classified as effective materials in the field of pollutant removal, due to their advanced porous structure which contributes to enhancing their ability to trap and remove various pollutants from the surrounding environment [15,16]. Furthermore, materials with nanoscale properties, such as silicon dioxide (SiO_2) particles, contribute to enhancing the efficiency of the adsorption process. Various types of nanomaterials have been employed in conjunction with hydrogels to improve adsorption performance and increase efficiency [17,18]. Furthermore, nano-oxides, such as SiO_2, have numerous applications in diverse fields including medicine, chemistry, thermal insulation, paints, and environmental science. These particles are widely used in water purification and pollutant removal due to their superior mechanical properties, large surface area, precise nanoscale size, high activity, ease of preparation, non-toxicity in aqueous environments, and favorable biocompatibility [19,20,21]. Researchers developed SiO_2-based hydrogels in which magnetic sodium alginate beads were used to effectively remove dyes and heavy metals. The results showed that the adsorption followed pseudo-second-order kinetics, with the process equilibrium time determined and the associated thermodynamic functions investigated [22-24]. The Sa-g-poly(AAM-co-CA)/SiO_2 nanocomposite was prepared using a Taguchi design to determine the optimal concentrations of monomers, sodium alginate, and initiating and binding agents. The nanocomposite underwent a series of analyses, including FTIR, FESEM, AFM, TEM, XRD, TGA, BET, and zero charge point determination. A comparative study with a hydrogel was also conducted to evaluate the effect of silica nanoparticles on adsorption, analyzing equilibrium time, effective weight, thermodynamics, kinetics, and the effects of pH, lead ion concentration, and temperature.

MATERIALS AND METHODS

Materials

Sodium alginate monomer (99% purity), silica nanoparticles (100% purity), and sodium hydroxide

(99% purity) were obtained from Sigma-Aldrich. Crotonic acid (99% purity) was obtained from CDH (India), while acrylamide, potassium persulfate (KPS), and the binding agent N,N'-methylene-bis-acrylamide (MBA) were all obtained in 99% purity from Macklin. Hydrochloric acid (HCl) was prepared in the laboratory and twice diluted with distilled water after being obtained in concentrated form from Fluka.

Synthesis of Sa-g-poly(AAM-co-CA)

Hydrogels were prepared by combining sodium alginate with acrylamide and crotonic acid, with free polymerization performed using KPS as a catalyst and MBA as a bonding agent. Nine hydrogel samples, as shown in Table 1, were used in the Taguchi $L9,3^4$ design using Minitab software [25]. Due to the effective role of silica nanoparticles in promoting bonding, they were added to investigate their effect on the swelling properties in water. To prepare the hydrogel, 0.15 g of sodium alginate was dissolved in 6 mL of distilled water at 50 °C for 40 minutes with continuous magnetic stirring until the monomer was completely dissolved, and then the temperature was reduced to room temperature. Next, 2 mL of a solution containing 1 g of acrylamide was gradually added with continuous stirring, followed by the addition of 0.2 g of crotonic acid dissolved in 2 mL of distilled water at 25 °C with continuous stirring. Then, 0.050 g of the binding agent MBA was added to the mixture with stirring, and finally 0.066 g of KPS as a polymerization catalyst under a continuous flow of nitrogen with stirring at 25 °C to ensure the formation of a stable and homogeneous hydrogel network.

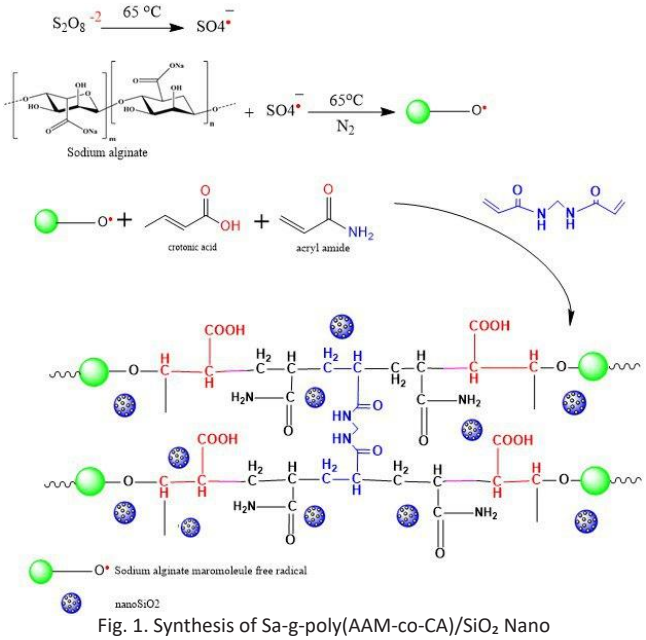

Fig. 1. Synthesis of Sa-g-poly(AAM-co-CA)/SiO_2 Nano

Table 1. Qe values based on Taguchi method for synthesis of Sa-g-poly(CA-AAM)/SiO_2.

No.	SiO_2	SA	Monomers	MBA %	KPS %	Qe
1	0.01	0.10	3	2.0	1.0	475.746
2	0.01	0.10	3	2.0	1.5	480.937
3	0.01	0.10	3	2.0	2.0	470.327
4	0.01	0.15	1	2.5	1.0	509.660
5	0.01	0.15	1	2.5	1.5	514.684
6	0.01	0.15	1	2.5	2.0	504.413
7	0.01	0.20	2	1.5	1.0	497.130
8	0.01	0.20	2	1.5	1.5	498.883
9	0.01	0.20	2	1.5	2.0	493.296

Synthesis of Sa-g-poly(AAM-co-CA)/SiO_2 Nano

The silica nanoparticle-containing hydrogel was prepared following the same protocol as the basic hydrogel preparation. 0.010 g of silica nanoparticles were dissolved in 2 mL of distilled water, and the mixture was then ultrasonically treated for 60 minutes to prevent clumping and ensure homogeneous particle dispersion. Subsequently, the silica nanoparticles were added to the hydrogel mixture after dissolving sodium alginate (in the second step before adding acrylamide). The mixture was placed in a water bath at 60 °C for three hours to form the Nano gel composite. After the reaction was complete, the nanocomposite was repeatedly cleaned with distilled water and then left to dry in a convection oven at 60 °C for two days. Finally, the dried nanocomposite was ground into a fine powder, as shown in Fig. 1.

Analysis and interpretation of the prepared sample

The prepared samples, comprising the Sa-g-poly(AAM-co-CA) hydrogel and the Sa-g-poly(AAM-co-CA)/SiO_2 nanocomposite, were analyzed using Fourier transform infrared spectroscopy (FTIR) in the 400–4000 cm^{-1} range, both before and after lead ion (Pb^{2+}) removal. The surface morphology of both the hydrogel and the nanocomposite was also investigated before and during lead ion adsorption using field emission scanning electron microscopy (FESEM), along with energy-dispersive X-ray spectroscopy (EDX) to determine the elemental distribution. Additionally, the samples underwent X-ray diffraction (XRD) analysis in the 0–80° range to evaluate the surface crystalline or semi-crystalline properties. To consider the harsh conditions that may contain some contaminants, the prepared nanocomposite and SiO_2 Nano particles were also examined using transmission electron microscopy (TEM). To assess the thermal stability of both the hydrogel and the nanocomposite, thermogravimetric analysis (TGA) was performed, and measurements were taken to determine the pore diameter, interfacial spaces, and surface area of both the hydrogel and the nanocomposite using multi-analytical methods (BET).

Experiments on absorption and swelling

The hydrogel's high swelling capacity upon hydration is one of the essential properties required for the preparation of the compound Sa-g-poly(AAM-co-CA)/SiO_2 Nano, as the amount of this swelling is a crucial factor in the efficiency of compound formation, which necessitated studying and highlighting this property in detail. Eq. 1 [26] was adopted to evaluate the swelling behavior of the compound Sa-g-poly(AAM-co-CA)/SiO_2 Nano within a wide range of pH values, ranging between 2–12, in order to study the effect of the acidic and basic medium on this property.

$$\text{Swelling}\,\% = (W_s - W_i) / W_i \times 100\,\% \quad (1)$$

Where: Wi : dry sample weight, Ws : weight of the sample after swelling

Zero point charge (PZC)

The electrical equilibrium point of the compound was determined using a 25 mL saline solution of NaCl (500 mg/L) at 25 °C, with pH values adjusted in the range of 2–12 using HCl and NaOH (0.1 and 1 M). 0.01 g of the compound was added to each solution, and the samples were shaken at 150 rpm for 1 hour [27]. After filtration, the pH of the filtrate was measured, and the initial and final values were plotted to accurately determine the electrical equilibrium point.

Adsorption study

To evaluate the effect of pH and ionic strength on the adsorption of lead ions (Pb^{2+}), experiments were conducted at 25 °C using 0.01 g of adsorbent per 10 mL of a 250 mg/L Pb^{2+} solution. The samples were shaken at 150 rpm to ensure equilibrium. The amount of adsorption was calculated using Eq. 2 [28].

$$Q_e = (C_0 - C_e) \times V / m \quad (2)$$

Where: C_0: original concentration of Pb^{2+}, Ce: pigment concentration at equilibrium, Qe: quantity of absorbent material, V: volume of absorbed solution (in litres), m: mass of absorbent material (in grams).

The removal ratio was calculated based on Eq. 3 [29], in order to evaluate the efficiency of the adsorbent in removing pollutant ions from the aqueous medium.

$$\text{Re}\,\% = (C_0 - C_e) / C_0 \times 100\,\% \quad (3)$$

The thermodynamic parameters for the adsorption of Pb^{2+}, which include ΔH, ΔS, ΔG, and

the equilibrium constant Keq, were calculated using appropriate Eqs. 4-6, with the aim of clarifying the nature of the adsorption process and determining its spontaneity [30].

$$\Delta G = - R T \ln K_{eq} \quad (4)$$

$$\ln K_{eq} = \Delta S / R - \Delta H / (R T) \quad (5)$$

$$K_C = C_a / C_e \quad (6)$$

R: universal gas constant, 8.314 $J \cdot mol^{-1} \cdot K^{-1}$, T: temperature (K), Ca: amount of adsorbate adsorbed at equilibrium.

Various equilibrium models, including the Langmuir Eq. 7, the Freundlich Eq. 8, and the Temkin Eq. 9, were applied to describe the adsorption behavior of Pb^{2+}. By calculating the correlation coefficients (R^2) and comparing their values, the most suitable model for representing the adsorption data was determined [31].

$$Q_e = Q_{max} K_L C_e / (1 + C_e K_L) \quad (7)$$

$$Q_e = K_f C_e^{1/n} \quad (8)$$

$$Q_e = B \ln (K_t C_e) \quad (9)$$

Where:, KL: Langmuir constant, Kf, n: Freundlich constants, B, Kt: Temkin constants, Qmax: the highest possible adsorption capacity.

Furthermore, a detailed study of the adsorption kinetics of Pb^{2+} was conducted, with solutions being sampled at predetermined time intervals. The adsorption of these samples was then measured using an atomic spectrometer, and the kinetic calculations were based on Eq. 10 for first-order quasi-analysis and Eq. 11 for second-order quasi-analysis to accurately determine the adsorption pattern and rate [32].

$$Q_t = Q_e (1 - e^{-K_1 t}) \quad (10)$$

$$Q_t = Q_e^2 K_2 t / (1 + K_2 Q_e t) \quad (11)$$

Qe: equilibrium absorption capacity, Qt: capacity for absorption at time t, K_1: pseudo-first-order absorption constant, K_2: pseudo-second-order absorption constant.

Comparison of the efficacy of adsorption

The efficiency of the hydrogel and the nanocomposite in removing Pb^{2+} at 25 °C was estimated using solutions with concentrations of 100–450 ppm, with the addition of 0.01 g of adsorbent to each solution. After shaking the solutions for 60 minutes, they were separated and the adsorption ratio for each substance was calculated.

RESULTS AND DISCUSSION

Characterization

FT-IR spectrum

The FTIR spectrum of sodium alginate monomer (Fig. 2a) shows a broad absorption band at 3214 cm^{-1} attributed to hydroxyl (OH) group vibrations. A band at 2929 cm^{-1} resulting from aliphatic (CH) bond vibrations is also observed. Furthermore, the strong, sharp bands associated with carbonyl (C=O) group vibrations indicate the monomer's characteristic chemical structure, with an additional band at 1303 cm^{-1} confirming the presence of this functional group [33,34]. The FTIR spectrum of SiO_2 nanoparticles (Fig. 2b) shows a broad band between 3414 and 3550 cm^{-1} attributed to Si–OH groups, and a band at 1633 cm^{-1} associated with surface water (Si–H_2O). Si–O vibrations are also observed at 1099 cm^{-1}, with additional symmetric bands at 808 and 470 cm^{-1}, illustrating the characteristic structure of the nanoparticles [35-37]. The FTIR spectrum of the hydrogel (Fig. 2c) shows carbonyl (C=O) group oscillations at 1712 cm^{-1} and carboxyl (COO^-) bands at 1452 and 1550 cm^{-1}. Bands of the amide (NH_2) group were also observed at 3351 and 3195 cm^{-1}, and an extension of (CH_2) at 2813 cm^{-1}, in addition to C=O oscillations within the amide and the extensions of the (C–C) and (C–N) groups at 1609 and 1430 cm^{-1}, respectively, demonstrating the integrated functional structure of the hydrogel [38-40]. The FTIR spectrum of the nanocomposite (Fig. 2d) shows novel bands compared to the hydrogel, resulting from the presence of SiO_2 nanoparticles. These include a Si–OH band at 3414 cm^{-1}, a Si–H_2O bend at 1633 cm^{-1}, as well as asymmetric Si–O–Si vibrations at 1095 cm^{-1} and symmetric bands at 808 and 470 cm^{-1}, demonstrating the structural interaction between the hydrogel and the nanoparticles. The FTIR spectrum of the nanocomposite after Pb^{2+} adsorption (Fig. 2e) shows a shift towards shorter wavelengths and weak absorption of the functional groups, due to their saturation with lead ions, which reduces their effectiveness in

absorbing infrared radiation [41].

FE-SEM / EDX explanation

FE-SEM images show that the hydrogel has a smooth texture and remarkable rigidity, with large pores resulting from the cross-linking network. When silica nanoparticles are incorporated to form the nanocomposite, structural changes become apparent as the nanoparticles fill the gaps within the network, enhancing rigidity and structural stability and creating a cohesive nanocomposite structure that supports better adsorption properties compared to the hydrogel alone. Fig. 3a shows that the nanocomposite network is more crystalline and porous than the hydrogel, which enhances its surface adsorption efficiency. Figs. 3b and 3c show the saturation of the outer surface of the adsorbent material with lead ions, with an increase in adsorption capacity and an increase in surface roughness as a result of the adhesion of the ions.

EDX analysis (Fig. 4) shows the difference in elemental composition between the hydrogel and the nanocomposite before and after Pb^{2+} adsorption. Silicon appears in the nanocomposite at 1.23 %, confirming the presence of SiO_2 nanoparticles, while a new lead peak of 15.46 % is recorded after adsorption, indicating the success of the adsorption process.

TEM explanation

The TEM image in Fig. 5a shows dark, semi-spherical SiO_2 nanoparticles clustered against a lighter background, a characteristic aggregation behavior of nanomaterials. When these particles

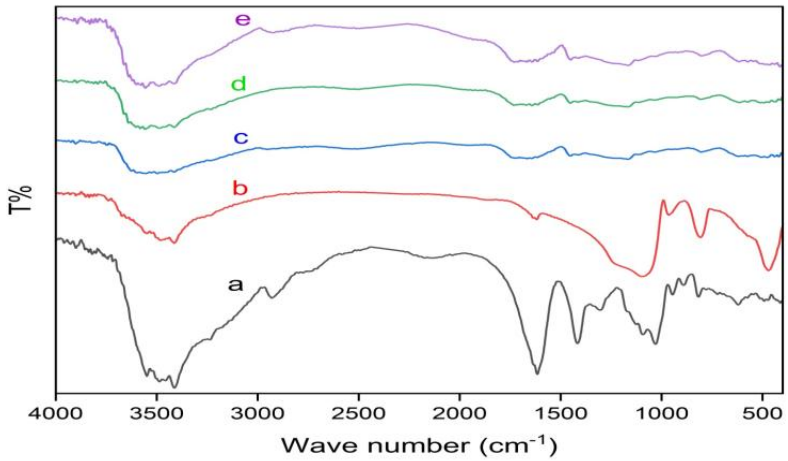

Fig. 2. FT-IR adsorption spectrum of (a) sodium alginate, (b) SiO_2 nano, (c) hydrogel, (d) nanocomposite, (e) nanocomposite after Pb^{2+} absorption.

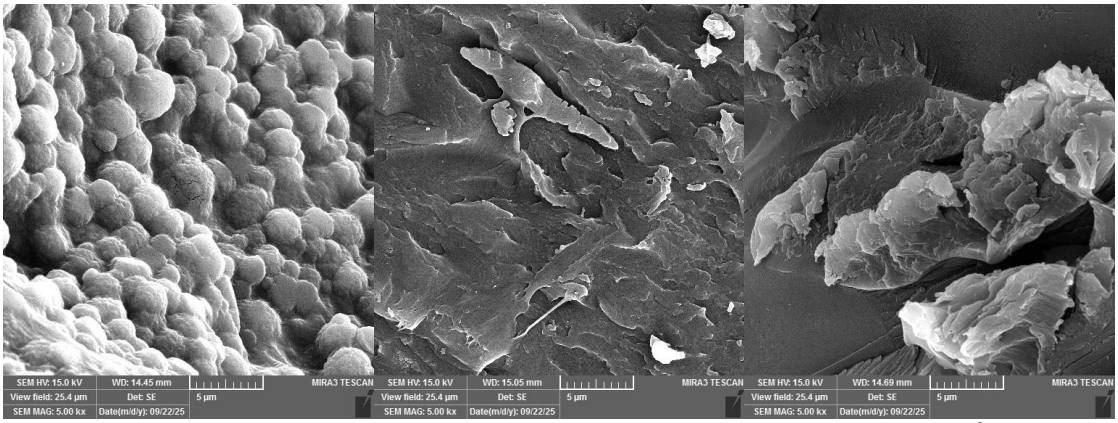

Fig. 3. FE-SEM images of (a) hydrogel, (b) nanocomposite, (c) nanocomposite after adsorption of Pb^{2+}.

are incorporated into the nanocomposite, as shown in Fig. 5b, irregular, semi-spherical aggregates form due to the non-uniform particle distribution and high electron density, reflecting the structural interaction between the hydrogel and the nanoparticles [42,43].

XRD concepts

Fig. 6 shows the X-ray diffraction (XRD) spectrum of the hydrogel, the nanocomposite, and the silica

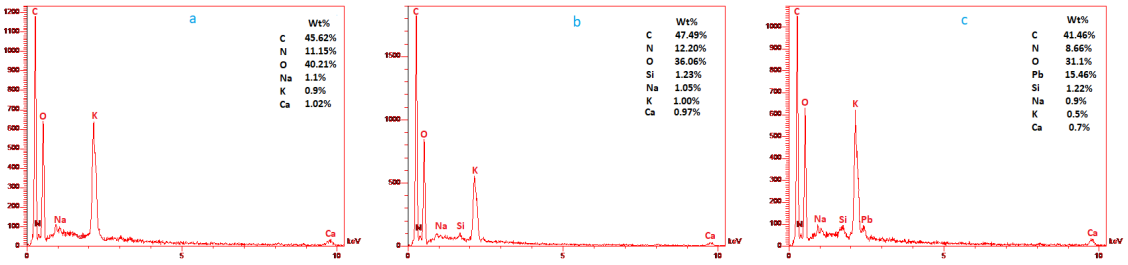

Fig. 4. EDX evaluation for (a) hydrogel, (b) nanocomposite, (c) nanocomposite after adsorption of Pb^{2+}.

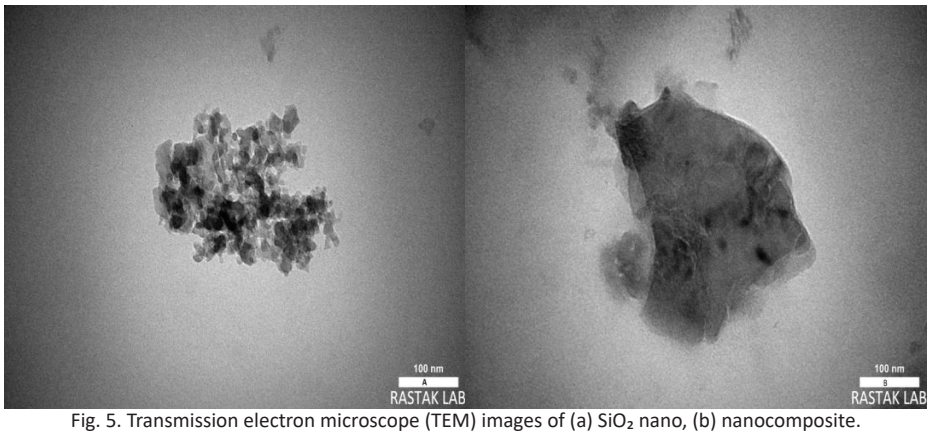

Fig. 5. Transmission electron microscope (TEM) images of (a) SiO_2 nano, (b) nanocomposite.

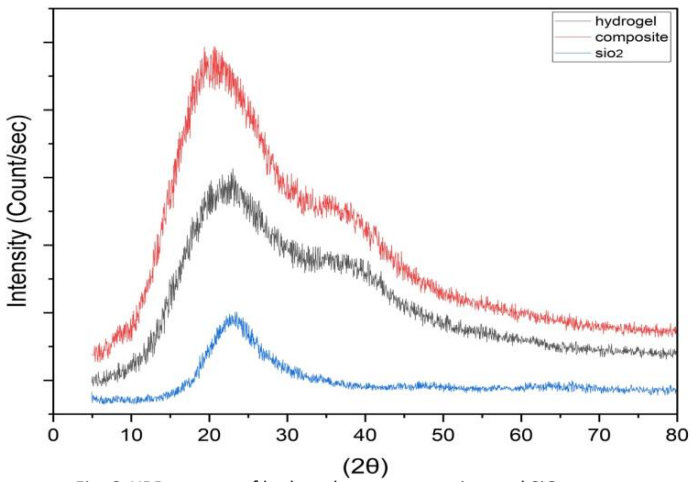

Fig. 6. XRD pattern of hydrogel, nanocomposite, and SiO_2 nano.

nanoparticles (SiO_2) in the solid state, using Cu-Kα light at a wavelength of 1.5106 Å within the 2θ angular range of 0–80° [44]. The hydrogel exhibits a broad band at 2θ = 22° (d = 4.04 Å), indicating its amorphous nature and the absence of crystalline phases. The nanocomposite shows a broad band at 2θ = 23° (d = 3.87 Å), while the silica nanoparticles exhibit a broad band at 2θ = 24° (d = 3.70 Å), also confirming their amorphous nature [45].

TGA principles

Figs. 7a and 7b show the thermal weight analysis (TGA) curves for both the hydrogel and the nanocomposite. The results indicate that the samples passed through four successive thermal phases. In the first phase (39.05–184.53 °C), a slight weight loss of 3.2084 % of the nanocomposite was recorded, resulting from the evaporation of physically absorbed water. This was followed by the second phase, within the range of 184.53–261.39 °C, which was associated with the decomposition of hydroxyl and carboxyl functional groups, resulting in a weight loss of 6.64235 %. The third phase (261.39–533.07 °C) represented the highest weight loss (47.63733 %), attributed to the decomposition of the nanocomposite's functional groups and the breakdown of the Si–OH groups of the SiO_2 nanoparticles. In the final stage, from 533.07 to 904.49 °C, complete

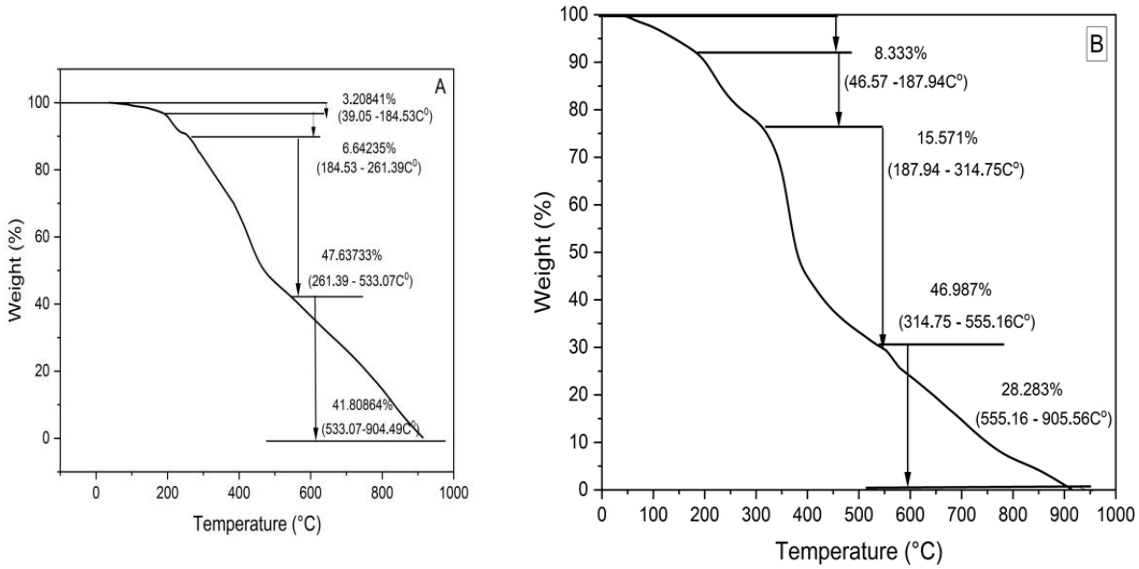

Fig. 7. Thermogravimetric analysis (TGA) of (a) nanocomposite and (b) hydrogel.

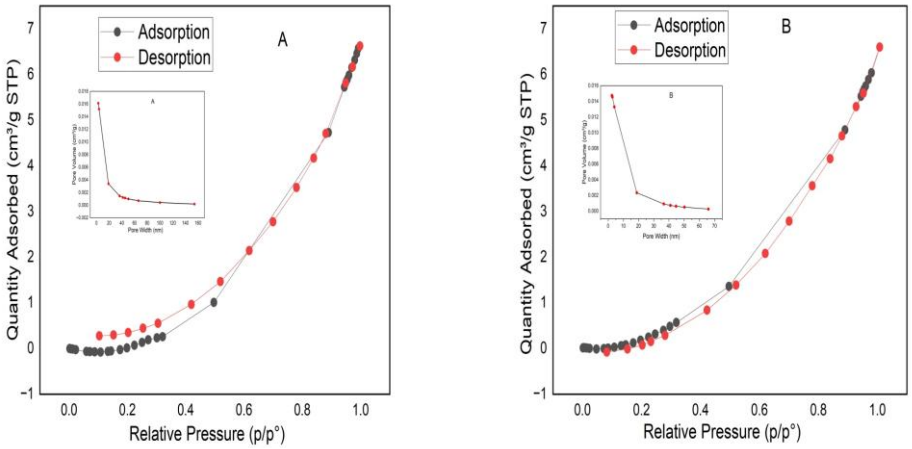

Fig. 8. Adsorption-desorption isotherms (BET-BJH) for (a) nanocomposite, (b) hydrogel.

thermal decomposition of the cross-linked polymer network occurred due to the breakdown of the carbon structure, accompanied by a weight loss of 41.80864 %. These results confirm that the incorporation of SiO_2 nanoparticles clearly contributed to enhancing the thermal stability of the nanocomposite compared to the hydrogel [46,47].

BET-BJH principles

Fig. 8 shows the adsorption-desorption curves of nitrogen gas for the nanocomposite and the hydrogel using the BET and BJH methods. Both samples exhibited type IV adsorption behavior, indicating a moderately porous structure with a uniform pore distribution. The nanocomposite had a surface area of 12.060 m^2/g, a pore volume of 0.016130 cm^3/g, and an average pore diameter of 5.3496 nm, while the hydrogel had a surface area of 11.901 m^2/g, a pore volume of 0.014743 cm^3/g, and an average pore diameter of 4.9552 nm. These results confirm that both materials possess moderate porosity suitable for adsorption processes, with the potential to improve efficiency by increasing the surface area and pore volume.

Point Zero Charge (PZC)

Fig. 9 illustrates the effect of pH on the surface charge of the adsorbent and its adsorption behavior by showing the relationship between pH and the zero-charge point (pHpzc). This point is a key criterion for understanding the behavior of magnetic hydrogels and their interaction with adsorbents based on the nature of their surface charge. The compound exhibited electrical neutrality at pH = 4.1, with its surface becoming

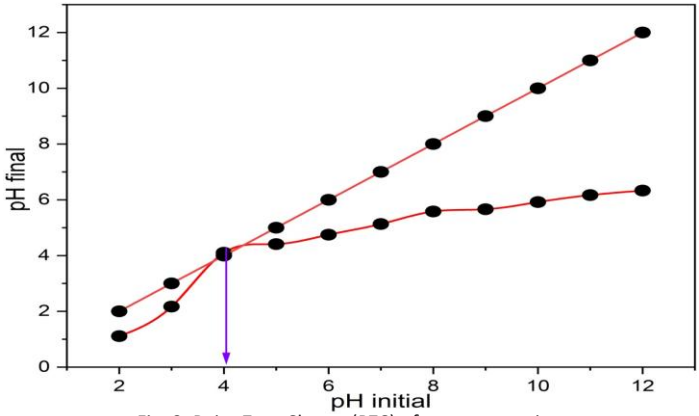

Fig. 9. Point Zero Charge (PZC) of nanocomposite.

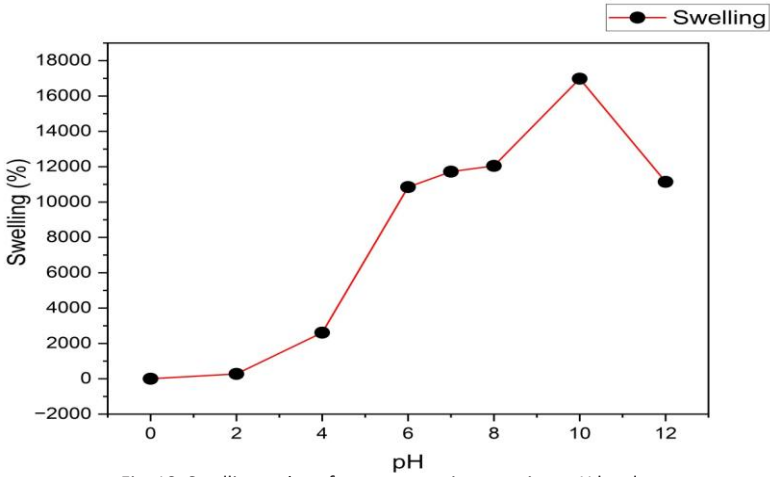

Fig. 10. Swelling ratios of nanocomposite at various pH levels.

negatively charged at values above this point, leading to increased swelling with increasing alkalinity. Conversely, at pH values below pHpzc, the surface acquires a positive charge due to the protonation of surface functional groups, such as hydroxyl and carboxyl groups, which causes the three-dimensional network structure of the compound to shrink [48]. These results are generally consistent with those reported in previous studies [49].

Swelling patterns

After immersion in aqueous solutions of varying pH values for 24 hours, the compound exhibited rapid water absorption and a marked increase in swelling, as illustrated in Fig. 10. This behavior is attributed to the ionization of hydrophilic groups such as hydroxyl and carboxyl groups, which become negatively charged at alkaline values. This ionization leads to repulsion between the polymer chains and opens the compound's network, allowing for the infiltration of more water molecules [50]. However, at pH 12, a decrease in swelling was observed due to the effect of positively charged sodium ions on the ionized carboxyl sites. This reduces the repulsion and limits the compound's ability to retain water.

Adsorption studies

Fig. 11 illustrates the effect of the adsorbent mass on adsorption capacity and removal efficiency. Increasing the weight improved the removal ratio while decreasing the capacity. At 0.01 g, the values were balanced and acceptable for both capacity and efficiency. Subsequent increases led to a decrease in capacity due to saturation of the active sites and clumping of the material; therefore, 0.01 g was adopted as the optimal weight for the experiments.

Fig. 12 illustrates the adsorption capacity

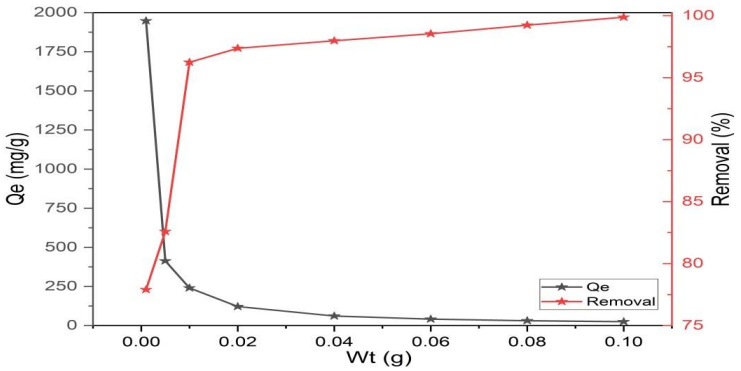

Fig. 11. Role of the adsorbent mass on the adsorption capacity and removal efficiency of Pb^{2+}.

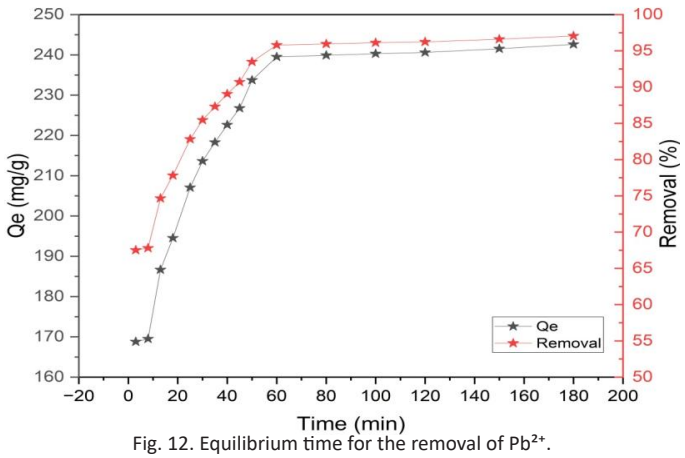

Fig. 12. Equilibrium time for the removal of Pb^{2+}.

and removal rate of Pb^{2+} ions over time. The adsorption process was rapid during the first three minutes due to the presence of empty active sites, then gradually stabilized over 60 minutes with no significant change in the removal rate. Therefore, an equilibrium time of 60 minutes was adopted for all experiments.

The effect of ionic strength on lead ion adsorption was investigated. The results, as shown in Fig. 13, indicate a decrease in both the removal rate and adsorption capacity in the presence of salts such as NaCl, KCl, and $CaCl_2$. This is attributed to competition between the positive ions of the salt and the lead ions for the negatively active sites of the adsorbent. As a result of this competition, the amount of lead adsorbed decreases, and the removal rate is reduced.

Fig. 14 shows the pH dependence of lead ion adsorption behavior at a concentration of 250 mg/L within the range of 2–10. A clear decrease in adsorption capacity and removal percentage was observed at values below the electrical equilibrium point (PZC = 4.1), attributed to the limited ionization of the active surface of the adsorbent. Conversely, exceeding the pH value of the electrical equilibrium point led to a significant improvement in adsorption performance, resulting from the ionization of active functional groups such as $Si–O^-$, COO^-, and CO^-, which strengthened the electrostatic attraction between the surface and the lead ions and contributed to increased removal efficiency [51].

Thermodynamic assessment

The effect of temperature on the adsorption of lead ions was investigated at temperatures ranging

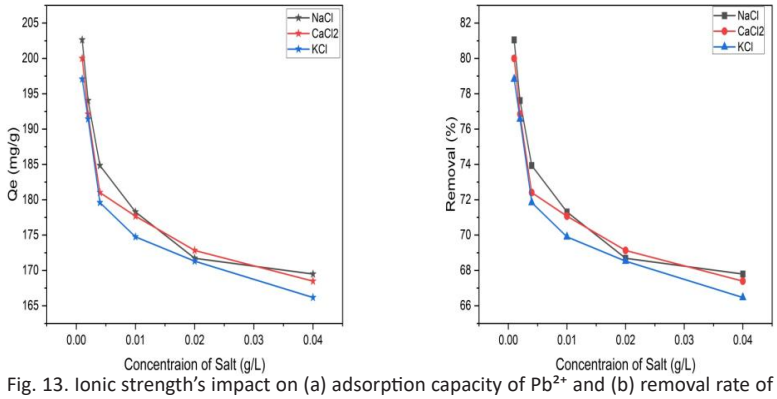

Fig. 13. Ionic strength's impact on (a) adsorption capacity of Pb^{2+} and (b) removal rate of Pb^{2+}.

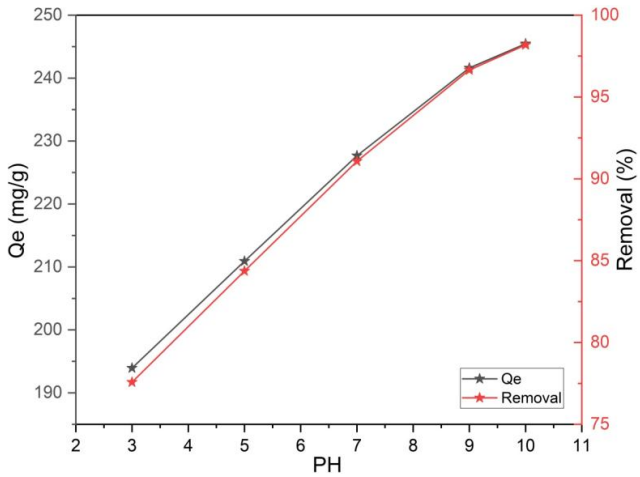

Fig. 14. Effect of pH on Pb^{2+} adsorption.

from 5 to 35 °C using different initial concentrations (150, 200, 250, 300, 350, 400 ppm). Fig. 15 shows a direct relationship between temperature and adsorption capacity, with the adsorption capacity increasing from 309.798 mg/L at 5 °C to 356.565 mg/L at 35 °C at a concentration of 400 ppm. These results indicate that the adsorption process on the silica nanoparticle-reinforced nanocomposite is endothermic in nature. This is attributed to improved ion mobility and increased interaction with active sites on the nanocomposite surface, in addition to the role of the porous structure in enhancing removal efficiency at high temperatures. The thermodynamic parameters

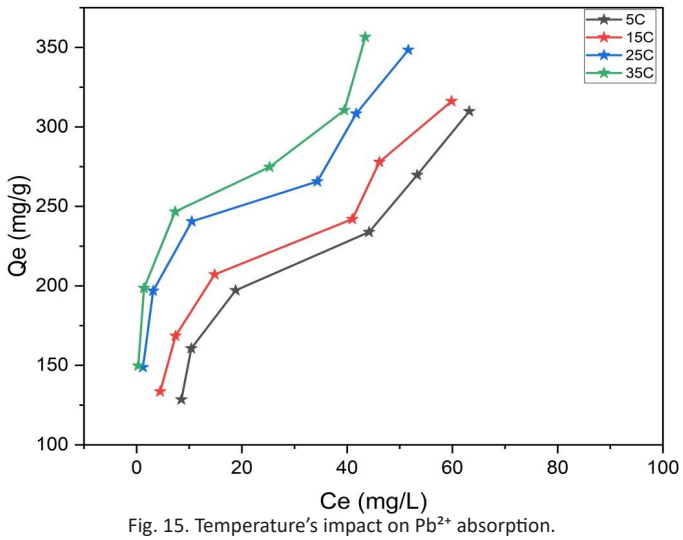

Fig. 15. Temperature's impact on Pb^{2+} absorption.

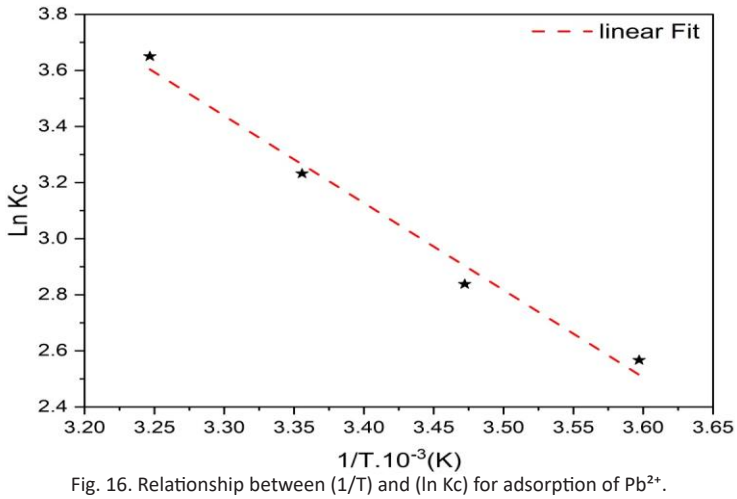

Fig. 16. Relationship between (1/T) and (ln Kc) for adsorption of Pb^{2+}.

Table 2. Thermodynamic function values for adsorption of Pb^{2+}.

T (K)	ΔG (kJ·mol^{-1})	ΔH (kJ·mol^{-1})	ΔS (J·mol^{-1}·K^{-1})	Kc
278	−5.932	25.852	113.902	13.0229
288	−6.795	—	—	17.0793
298	−8.008	—	—	25.3324
308	−9.347	—	—	38.4758

(ΔG, ΔH, ΔS) were also evaluated to elucidate the adsorption mechanism in the aqueous medium [52,53].

The data indicate that the changes in enthalpy (ΔH) and entropy (ΔS) are positive, demonstrating that adsorption is endothermic and involves an increase in the orderliness of the system during the transition from the solution to the solid phase. Furthermore, the Gibbs free energy (ΔG) becomes more negative with increasing temperature, reflecting the thermal suitability of the process.

Kinetics and isotherm mechanism

The adsorption kinetics of lead ion at 25 °C and an initial concentration of 250 mg/L were investigated to determine the time to equilibrium. The results obtained from applying the two nonlinear equations showed high agreement with the pseudo-second-order model, with the adsorption capacity at equilibrium reaching 240.505 mg/g, which is very close to the theoretical value predicted by this model, as shown in Table 3 and Fig. 17.

The value of Qe(cal) for the pseudo-second-order reaction model was 242.0650 mg/g with a higher correlation coefficient (R^2 = 0.9677) compared to the pseudo-first-order model, which showed a lower correlation coefficient (R^2 = 0.4141) and a Qe(cal) value less consistent with experimental values. Therefore, the adsorption process better follows the pseudo-second-order reaction model.

The equilibrium data were subjected to the Langmuir, Freundlich, and Temkin models (Fig. 18). The results showed the Langmuir model to be superior in terms of correlation coefficient at different temperatures, followed by the Temkin model with a high degree of agreement, while the Freundlich model was the least favorable. Table 4 shows the model coefficients and R^2 values, allowing for a quantitative assessment of their accuracy in describing the adsorption behavior. The data indicate multilayer adsorption with a physical nature to the process, which is consistent

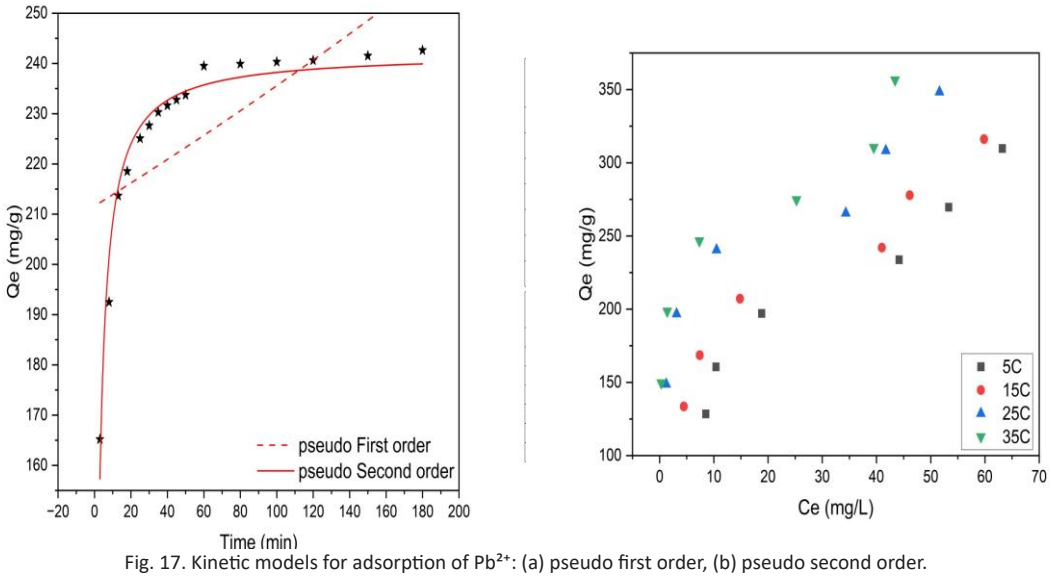

Fig. 17. Kinetic models for adsorption of Pb^{2+}: (a) pseudo first order, (b) pseudo second order.

Table 3. Kinetic function and constant values for the absorption of Pb^{2+}.

Model	Parameter	Value
Pseudo first order	K_1	0.00107
Pseudo first order	Qe (cal) (mg/g)	211.619
Pseudo first order	R^2	0.4141
Pseudo second order	K_2	0.00256
Pseudo second order	Qe (cal) (mg/g)	242.065
Pseudo second order	R^2	0.9677

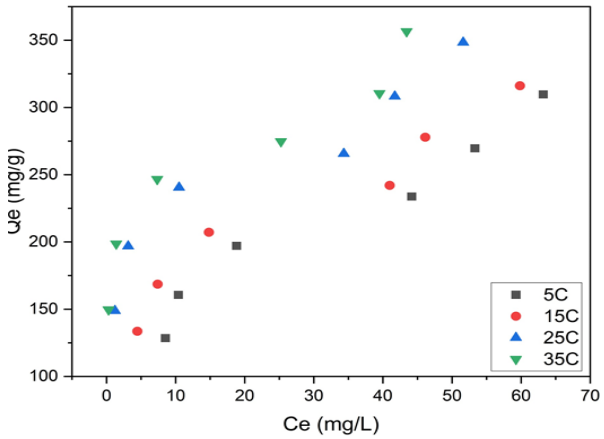

Fig. 19. Comparison of adsorption performance (removal efficiency and capacity) for hydrogel and nanocomposite materials toward Pb^{2+}.

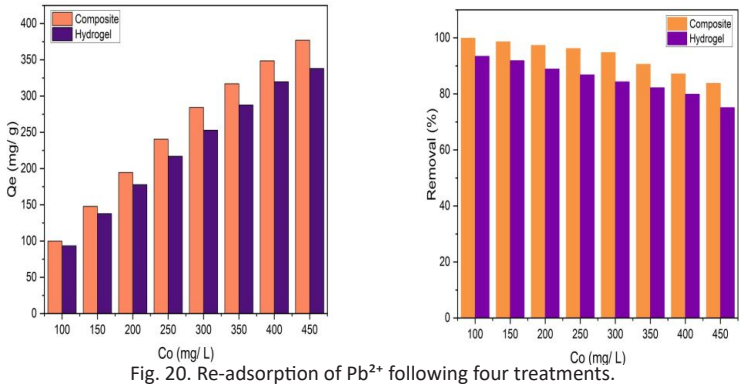

Fig. 20. Re-adsorption of Pb^{2+} following four treatments.

Table 4. Isothermal factors for adsorption of Pb^{2+} on the surface of the nanocomposite.

Langmuir eq.			Freundlich eq.			Temkin eq.		
R^2	Qmax	KL	R^2	n	Kf	R^2	B	Kt
0.9247	344.942	0.0723	0.2203	0.9919	5.4014	0.9406	75.9070	0.6921

with the previously calculated enthalpy values.

Adsorption comparison between nanocomposite and hydrogel

The adsorption process was studied at initial lead ion concentrations ranging from 100 to 450 mg/L, at 25 °C and pH 7. 0.01 g of both the hydrogel and the nanocomposite loaded with SiO_2 nanoparticles were used, with shaking for 60 minutes to ensure equilibrium. The results showed that the nanocomposite exhibited superior adsorption efficiency compared to the unmodified material, attributed to its increased surface area and number of active sites, as illustrated in Fig. 19.

Reusability study

The nanocomposite material was reactivated by washing with a 1 M NaOH solution and then drying for reuse. The results (Fig. 20) showed that it retained good efficiency during four adsorption cycles. At a concentration of 250 mg/L Pb^{2+}, the adsorption capacity decreased from 233.131 to 177.575 mg/g after the fourth cycle, indicating acceptable stability and efficient reuse potential supported by Nano silica [54,55].

CONCLUSION

SA-g-poly(AAM-co-CA) hydrogel was prepared using free-radical polymerization with a Taguchi

design to determine the optimal concentrations of the system components. Its structure was further enhanced by the addition of SiO_2 nanoparticles to obtain a nanocomposite. Swelling tests at different pH values showed the superiority of the nanocomposite hydrogel, with a maximum swelling of 16978.57 % at pH = 10, compared to 11143.75 % for the unsupported hydrogel at pH = 12. This confirms the role of Nano silica in improving water adsorption capacity. In Pb^{2+} removal applications, the nanocomposite exhibited a higher adsorption capacity (376.969 mg/g) compared to the hydrogel (337.979 mg/g), attributed to the increased density of active sites and improved surface properties. The equilibrium time was set to 60 minutes, and the kinetic analysis showed good agreement with the pseudo-second-order model, indicating that the adsorption process is governed by the nature of the active sites. The thermal data showed that the adsorption was endothermic (ΔH = 25.852 kJ/mol) with increased randomness at the interface (ΔS = 113.901 J/mol·K), while the negative ΔG values (−8.007 kJ/mol at 25 °C) confirmed the spontaneity of the process, with performance improving with increasing temperature. From a modeling perspective, the compound showed better agreement with the Langmuir model, indicating the formation of a monolayer on a semi-homogeneous surface, while the Freundlich model showed limited agreement. The Temkin model provided a good fit, reflecting the influence of the adsorption energy and the distribution of the active sites.

ACKNOWLEDGMENTS

The authors express their sincere gratitude to Al-Qadisiyah University, Iraq, for providing the necessary laboratory facilities and equipment for this study. They also thank the laboratory team for their support and effective cooperation throughout all stages of the work.

CONFLICT OF INTEREST

The authors declare that there is no conflict of interests regarding the publication of this manuscript.

REFERENCES

1. Alhamd SJ, Abbas MN, Manteghian M, Ibrahim TA, Jarmondi KDS. Treatment of Oil Refinery Wastewater Polluted by Heavy Metal Ions via Adsorption Technique using Non-Valuable Media: Cadmium Ions and Buckthorn Leaves as a Study Case. Karbala International Journal of Modern Science. 2024;10(1).
2. Oladipo AA, Ahaka EO, Gazi M. High adsorptive potential of calcined magnetic biochar derived from banana peels for Cu^{2+}, Hg^{2+}, and Zn^{2+} ions removal in single and ternary systems. Environmental Science and Pollution Research. 2019;26(31):31887-31899.
3. Rahman A. Promising and Environmentally Friendly Removal of Copper, Zinc, Cadmium, and Lead from Wastewater Using Modified Shrimp-Based Chitosan. Water. 2024;16(1):184.
4. Pérez-Marín AB, Zapata VM, Ortuño JF, Aguilar M, Sáez J, Lloréns M. Removal of cadmium from aqueous solutions by adsorption onto orange waste. J Hazard Mater. 2007;139(1):122-131.
5. Gudadhe S, Singh SK, Ahsan J. Cellular and Neurological Effects of Lead (Pb) Toxicity. Environmental Contamination Remediation and Management: Springer Nature Switzerland; 2024. p. 125-145.
6. Ma L, Liu J-Y, Dong J-X, Xiao Q, Zhao J, Jiang F-L. Toxicity of Pb^{2+} on rat liver mitochondria induced by oxidative stress and mitochondrial permeability transition. Toxicol Res. 2017;6(6):822-830.
7. Lalwani P, King DE, Morton KS, Rivera NA, Huayta J, Hsu-Kim H, et al. Increased cytotoxicity of Pb^{2+} with co-exposures to a mitochondrial uncoupler and mitochondrial calcium uniporter inhibitor. Environmental Science: Processes and Impacts. 2023;25(11):1743-1751.
8. Tolkou AK, Tsoutsa EK, Kyzas GZ, Katsoyiannis IA. Sustainable use of low-cost adsorbents prepared from waste fruit peels for the removal of selected reactive and basic dyes found in wastewaters. Environmental Science and Pollution Research. 2024;31(10):14662-14689.
9. Melese H, Tsade H. Cellulose based adsorbent for cationic methylene blue dye removal. Discover Applied Sciences. 2024;6(2).
10. Bellaj M, Yazid H, Aziz K, Regti A, Haddad ME, Achaby ME, et al. Eco-friendly synthesis of clay-chitosan composite for efficient removal of alizarin red S dye from wastewater: A comprehensive experimental and theoretical investigation. Environ Res. 2024;247:118352.
11. Dalalibera A, Vilela PB, Vieira T, Becegato VA, Paulino AT. Removal and selective separation of synthetic dyes from water using a polyacrylic acid-based hydrogel: Characterization, isotherm, kinetic, and thermodynamic data. Journal of Environmental Chemical Engineering. 2020;8(5):104465.
12. Hemeda ES, Bashandy AA, Nasser AA. Improving Mechanical Properties of Recycled Aggregate Pervious Concrete Using Taguchi Method. Civil and Environmental Engineering. 2024;20(2):1186-1202.
13. Kulkarni GS, Siddeshkumar NG, Prasad CD, Shankar BL, Aprameya CR, Patane P, et al. Synthesis and Investigation on Mechanical Properties of Hybrid FRP Composite Using Taguchi Technique. Journal of The Institution of Engineers (India): Series D. 2024;106(2):889-903.
14. Oladipo AA, Gazi M. Fixed-bed column sorption of borate onto pomegranate seed powder-PVA beads: a response surface methodology approach. Toxicological and Environmental Chemistry. 2014;96(6):837-848.
15. Yang L, Bao L, Zhong Y, Hao C, Chen J, Wu J, et al. Fabrication of in situ metal-organic framework grown on sodium lignosulphonate hydrogel for removal of Pb^{2+}, methylene blue and crystal violet from aqueous solution. Journal of Cleaner Production. 2024;434:139831.

16. Ahmadi S, Pourebrahimi S, Malloum A, Pirooz M, Osagie C, Ghosh S, et al. Hydrogel-based materials as antibacterial agents and super adsorbents for the remediation of emerging pollutants: A comprehensive review. Emerging Contaminants. 2024;10(3):100336.
17. Du X, Gu S, Wang X, Zhang S, Zhang B, Yu G, et al. The preparation of SiO_2/GO/PVA based hydrogel sensor and its application for rapid and sensitive detection of NH_3. Sensors Actuators B: Chem. 2025;424:136885.
18. Long X, Yu H, Zhang P, Qian C, Lu M, Fu Y. Dimensionally stable thermal-stiffening composite hydrogels enabled by thermo-responsive SiO_2 hybrid nanoparticles. Colloids Surf Physicochem Eng Aspects. 2025;709:136129.
19. Soliman TS, Vshivkov SA, Elkalashy SI. Structural, thermal, and linear optical properties of SiO_2 nanoparticles dispersed in polyvinyl alcohol nanocomposite films. Polym Compos. 2020;41(8):3340-3350.
20. Oukebdane K, Necer IL, Didi MA. Binary comparative study adsorption of anionic and cationic Azo-dyes on Fe_3O_4-Bentonite magnetic nanocomposite: Kinetics, Equilibrium, Mechanism and Thermodynamic study. Silicon. 2022;14(15):9555-9568.
21. Seema, Kumar N, Chand S. Structural, morphological, optical and dielectric properties of $Ti_{1-x}Fe_xO_2$ nanoparticles synthesized using sol-gel method. J Sol-Gel Sci Technol. 2022;105(1):163-175.
22. Chen S, Wen H, Zheng T, Liu X, Wang Z, Tian S, et al. Engineering sodium alginate-SiO_2 composite beads for efficient removal of methylene blue from water. Int J Biol Macromol. 2023;239:124279.
23. Xiao Y, Wang L, Zhang X, Ren Y, Wang J, Niu B, et al. Preparation and Characterization of Silica-Coated Sodium Alginate Hydrogel Beads and the Delivery of Curcumin. J Biomater Sci Polym Ed. 2024;35(14):2153-2169.
24. Hussain S, Salman M, Al-Ahmary KM, Ahmed M. Synthesis of potential adsorbent for removal of malachite green dye using alginate hydrogel nanocomposites. Int J Biol Macromol. 2025;289:138816.
25. Estrada-Vázquez R, Vaca-Mier M, Bustos-Terrones V, Rangel-Peraza JG, Loaiza JG, Hermosillo-Nevárez JJ, et al. Degradation of agricultural pollutants by biopolymer-enhanced photocatalysis: application of Taguchi method for optimization. Reaction Kinetics, Mechanisms and Catalysis. 2023;137(1):523-545.
26. Noor AA, Radia ND. Optimization of Pb^{2+} adsorption onto Fe_3O_4/sodium alginate-grafted magnetic hydrogel using RSM: synthesis optimization via taguchi method. J Porous Mater. 2025;32(5):1879-1899.
27. Chaudhary J, Thakur S, Mamba G, Prateek, Gupta RK, Thakur VK. Hydrogel of gelatin in the presence of graphite for the adsorption of dye: Towards the concept for water purification. Journal of Environmental Chemical Engineering. 2021;9(1):104762.
28. Ibrahim BM, Fakhre NA, Jalhoom MG, Qader IN, Shareef HY, Jalal AF. Removal of lead ions from aqueous solutions by modified cellulose. Environ Technol. 2022;45(12):2335-2347.
29. Vo LQ, Vu A-T, Le TD, Huynh CD, Tran HV. Fe_3O_4/Graphene Oxide/Chitosan Nanocomposite: A Smart Nanosorbent for Lead(II) Ion Removal from Contaminated Water. ACS Omega. 2024.
30. Ameen kaka Mohammed A, Jibrael Al-Salihi KJ, HamaRawf RF. Synthesis, characterization, and application of low-cost Mg-Al/CO_3 and Ni-Al/CO_3 layered double hydroxides (LDHs) as adsorbents for the removal of aniline blue dye from aqueous solutions: adsorption isotherms, kinetics, and thermodynamic studies. RSC Advances. 2025;15(34):27630-27641.
31. Madankar R, Umekar M, Bhusari G, Mondal A, Raish M, Afzal M, et al. Rapid synthesis of graphitic carbon nitride nanosheets as an efficient adsorbent for removal of Methylene Blue and Rhodamine B from Aqueous Solutions. Sci Rep. 2025;15(1).
32. Holliday MC, Parsons DR, Zein SH. Agricultural Pea Waste as a Low-Cost Pollutant Biosorbent for Methylene Blue Removal: Adsorption Kinetics, Isotherm And Thermodynamic Studies. Biomass Conversion and Biorefinery. 2022;14(5):6671-6685.
33. Mehra M, Sheorain J, Bakshi J, Grewal S, Dhingra D, Bernela M, et al. Sodium alginate polymer nanoformulation as promising carrier for berberine delivery: Synthesis, morphology and in-vitro evaluation. Carbohydrate Polymer Technologies and Applications. 2024;7:100408.
34. Oladipo AA, Gazi M, Saber-Samandari S. Adsorption of anthraquinone dye onto eco-friendly semi-IPN biocomposite hydrogel: Equilibrium isotherms, kinetic studies and optimization. Journal of the Taiwan Institute of Chemical Engineers. 2014;45(2):653-664.
35. Varpe AS, Deshpande MD. Study of structural, optical, and dielectric properties of sol–gel derived ZnFe2O4–Al2O3 composite nanoparticles. J Sol-Gel Sci Technol. 2020;96(3):718-727.
36. Praseptiangga D, Zahara HL, Widjanarko PI, Joni IM, Panatarani C. Preparation and FTIR spectroscopic studies of SiO_2-ZnO nanoparticles suspension for the development of carrageenan-based bio-nanocomposite film. AIP Conference Proceedings: AIP Publishing; 2020. p. 100005.
37. Ajji Z, Maarouf M, Khattab A, Ghazal H. Synthesis of pH-responsive hydrogel based on PVP grafted with crotonic acid for controlled drug delivery. Radiat Phys Chem. 2020;170:108612.
38. Du C, Song Y, Shi S, Jiang B, Yang J, Xiao S. Preparation and characterization of a novel Fe_3O_4-graphene-biochar composite for crystal violet adsorption. Sci Total Environ. 2020;711:134662.
39. Batouti ME, Sadik W, Eldemerdash AG, Hanafy E, Fetouh HA. New and innovative microwave-assisted technology for synthesis of guar gum-grafted acrylamide hydrogel superabsorbent for the removal of acid red 8 dye from industrial wastewater. Polym Bull. 2022;80(5):4965-4989.
40. Saber-Samandari S, Gazi M, Yilmaz E. UV-induced synthesis of chitosan-g-polyacrylamide semi-IPN superabsorbent hydrogels. Polym Bull. 2011;68(6):1623-1639.
41. Zheng Y, Ye H, Zhao G, Rao H, Liu H, Liu F, et al. Competitive adsorption and correlative mechanism of heavy metal ions using ploy(cellulose/humic acid/acrylic acid) in multi-element aqueous medium. Polym Bull. 2020;78(5):2523-2535.
42. Niu F, Wang X, Yang S, Xu S, Zhang Y, Suga T, et al. Low-temperature Cu/SiO_2 hybrid bonding based on Ar/H2 plasma and citric acid cooperative activation for multi-functional chip integration. Appl Surf Sci. 2024;648:159074.
43. Chen S, Gueddida S, Badawi M, Lebègue S, Giraudon J-M, Dhainaut J, et al. Unravelling the critical role of silanol in Pt/SiO_2 for room temperature HCHO oxidation: An experimental and DFT study. Applied Catalysis B:

Environmental. 2023;331:122672.
44. Synthesis of Nanosized Titanium Dioxide (TiO_2) by Sol-Gel Method. International Journal of Innovative Technology and Exploring Engineering. 2019;9(2S2):732-735.
45. Rahimzadeh CY, Barzinjy AA, Mohammed AS, Hamad SM. Green synthesis of SiO_2 nanoparticles from Rhus coriaria L. extract: Comparison with chemically synthesized SiO_2 nanoparticles. PLoS One. 2022;17(8):e0268184.
46. Zoccal JVM, Arouca FO, Gonçalves JAS. Synthesis and Characterization of TiO_2 Nanoparticles by the Method Pechini. Mater Sci Forum. 2010;660-661:385-390.
47. Hazel D, Gobi N. One-Pot Facile Green Synthesis of Iron Oxide Nanoparticles Using Aqueous Stem Extract of Amaranthus Campestris and Comparison of its Characteristics with Chemically Synthesized Iron Oxide Nanoparticles. Springer Science and Business Media LLC; 2022.
48. Wang Z, Muhammad Y, Tang R, Lu C, Yu S, Song R, et al. Dually organic modified bentonite with enhanced adsorption and desorption of tetracycline and ciprofloxacine. Sep Purif Technol. 2021;274:119059.
49. Ibrahim MA, Jaafar MZ, Yusof MAM, Shye CA, Idris AK. Influence of size and surface charge on the adsorption behaviour of silicon dioxide nanoparticles on sand particles. Colloids Surf Physicochem Eng Aspects. 2023;674:131943.
50. Liu H, Liu M, Zhang L, Ma L, Chen J, Wang Y. Dual-stimuli sensitive composites based on multi-walled carbon nanotubes and poly(N,N-diethylacrylamide-co-acrylic acid) hydrogels. React Funct Polym. 2010;70(5):294-300.
51. Obsa AL, Shibeshi NT, Mulugeta E, Workeneh GA. Eco-friendly composite hydrogel based on cellulose and bentonite for removal of lead (II): Kinetics and isotherm studies. Carbohydrate Polymer Technologies and Applications. 2025;9:100637.
52. Wang B, Yin H, Zhang M, Zhang F. Efficient removal of Pb(II) and Cd(II) from water by polyethyleneimine-amidated sepiolite-sodium alginate composite microspheres: Characterization and mechanistic analysis. Journal of Industrial and Engineering Chemistry. 2025;143:617-631.
53. Ayaa Ahmed S, Layth SJ. Eco-friendly hydrogel based on carboxymethylcellulose poly (acrylic acid-co-hydroxyethyl acrylamide) (CMC-AAC-co-HEAM) for sustainable removal of Pb (II) ions from contaminated water. Applied Chemical Engineering. 2025.
54. Samy A, Ismail AM, Ali H. Environmentally friendly mesoporous SiO_2 with mixed fiber/particle morphology and large surface area for enhanced dye adsorption. Journal of Materials Science. 2023;58(4):1586-1607.